

# Path Integral Monte Carlo and Density Functional Molecular Dynamics Simulations of Hot, Dense Helium

B. Militzer

*Departments of Earth and Planetary Science and Astronomy,  
University of California, Berkeley, CA 94720, USA*

(Dated: April 26, 2019)

Two first-principles simulation techniques, path integral Monte Carlo (PIMC) and density functional molecular dynamics (DFT-MD), are applied to study hot, dense helium in the density-temperature range of  $0.387 - 5.35 \text{ g cm}^{-3}$  and  $500 \text{ K} - 1.28 \times 10^8 \text{ K}$ . One coherent equation of state (EOS) is derived by combining DFT-MD data at lower temperatures with PIMC results at higher temperatures. Good agreement between both techniques is found in an intermediate temperature range. For the highest temperatures, the PIMC results converge to the Debye-Hückel limiting law. In order to derive the entropy, a thermodynamically consistent free energy fit is introduced that reproduces the internal energies and pressure derived from the first-principles simulations. The equation of state is presented in form of a table as well as a fit and is compared with chemical models. In addition, the structure of the fluid is analyzed using pair correlation functions. Shock Hugoniot curves are compared with recent laser shock wave experiments.

## I. INTRODUCTION

After hydrogen, helium is the second most common element in the universe. While it rarely occurs in pure form in nature, it is an endmember of hydrogen-helium mixtures (HHM) that are the prevalent component in solar and extrasolar giant gas planets. The characterization of helium's properties at extreme temperature and pressure conditions is therefore important to study planetary interiors and especially relevant for answering the question whether HHM phase-separate in giant planet interiors<sup>1,2</sup>. In most planetary models, the equation of state (EOS) of HHM was inferred from the linear mixing approximation at constant pressure and temperature using the EOSs of pure hydrogen and helium. The latter is the central topic of this article.

Hydrogen and helium share some common properties. Both are very light and exhibit rich quantum properties at low temperature. More importantly for this paper, the helium atom and the deuterium molecule have similar masses and both have two elemental excitation mechanisms that determine their behavior at high temperature. The helium atom has two ionization stages while deuterium molecules can dissociate and the resulting atoms can be ionized. However, helium is without question simpler to characterize at high pressure. The crystal structure is hexagonal closed-packed under most  $(P, T)$  conditions<sup>3,4</sup> while in solid hydrogen, different degrees of molecular rotational ordering lead to several phases that deviate from the h.c.p. structure. Hydrogen is expected to turn metallic at a few hundred GPa while a much larger bandgap must be closed in helium, which is predicted to occur above  $10\,000 \text{ GPa}$ <sup>5,6</sup>.

Given the relative simplicity of helium's high pressure properties one expects that there would be less of a controversy in the EOS than for hydrogen. This makes helium a good material to test novel experimental and theoretical approaches. For hydrogen, the first laser shock experiments that reached megabar pressures had pre-

dicted that the material would be highly compressible under shock conditions and reach densities six times higher than initial state<sup>7,8</sup>. Later experiments<sup>9,10,11,12</sup> showed reduced compression ratios close to 4.3, which were in good agreement with first-principles calculations<sup>13,14,15</sup>. In the case of helium, there is very good agreement between the early shock experiments by Nellis *et al.*<sup>16</sup> and first-principles calculation<sup>17</sup>.

Recently the first laser shock experiments were performed on precompressed helium samples<sup>18</sup>. The measurements confirmed the theoretically predicted trend<sup>17</sup> that the shock compression ratio is reduced with increasing precompression. However, there is discrepancy in the magnitude of the compression. Shock measurements<sup>18</sup> without precompression showed compression ratios of about 6 while first-principles simulation<sup>17</sup> predicted only  $5.24(4)$ . The discrepancy between theoretical and experimental predictions is reduced for higher precompressions. For samples that were precompressed to 3.4-fold the ambient density, theory and experiment are in agreement.

The properties of fluid helium change from hard-sphere liquid at low pressure and temperature to ultimately a two-component plasma, after ionization has occurred at high pressure and temperature. The associated insulator-to-metal transition has been the topic of three recent theoretical studies that all relied on DFT methods. Kietzmann *et al.*<sup>19</sup> studied the rise in electrical conductivity using the Kubo-Greenwood formula and compared with shock-wave experiments by Ternovoi *et al.*<sup>20</sup>. Kowalski *et al.*<sup>6</sup> studied dense helium in order to characterize the atmosphere of white dwarfs. This paper went beyond the generalized gradient approximation by considering hybrid functionals. Stixrude and Jeanloz<sup>21</sup> studied the band gap closure in the dense fluid helium at over a wide range of densities including conditions of giant planet interiors.

This article provides the EOS for fluid helium over a wide range of temperatures ( $500 \text{ K} - 1.28 \times 10^8 \text{ K}$ ) and densities ( $0.387 - 5.35 \text{ g cm}^{-3}$  corresponding to a Wigner-Seitz

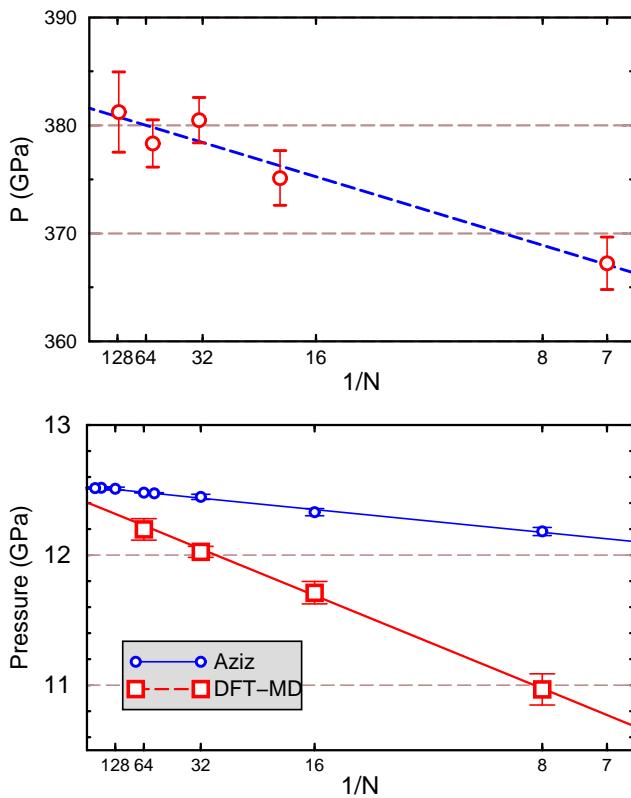


FIG. 1: The upper panel shows the finite size dependence of the pressure as function of the number atoms,  $N$ , as predicted from PIMC simulations with free-particle nodes at  $T=125\,000$  K and  $r_s = 1.86$ . The lower panel compares the finite size dependence of DFT-MD simulations and classical Monte Carlo calculations using the Aziz pair potential at  $T=10\,000$  K and  $r_s = 2.4$ .

radius interval of  $r_s=2.4-1.0$  where  $\frac{4}{3}\pi r_s^3 = V/N_e$  by combining two first-principles simulation methods, path integral Monte Carlo (PIMC) at higher temperatures with density functional molecular dynamics (DFT-MD) at lower temperatures. The temperature range was significantly extended compared to our earlier work<sup>17</sup> that focused exclusively on shock properties alone. Here, the region of validity of both first-principles methods is analyzed and good agreement for EOS at intermediate temperatures is demonstrated. The PIMC calculations have been extended to much higher temperatures until good agreement with the Debye-Hückel limiting law is found. In the density interval under consideration, the entire EOS of nonrelativistic, fluid helium has been mapped out from first principles. All EOS data are combined into one thermodynamically consistent fit for the free energy and the entropy is derived. The structure of the fluid is analyzed using pair correlation functions and, finally, additional results for shock Hugoniot curves are presented.

## II. METHODS

Path integral Monte Carlo<sup>22</sup> is the most appropriate and efficient first-principles simulation techniques for quantum system with thermal excitations. Electrons and nuclei are treated equally as paths, although the zero-point motion of the nuclei as well as exchange effects are negligible for the temperatures under consideration. The Coulomb interaction between electrons and nuclei is introduced using pair density matrices that we derived using the eigenstates of the two-body Coulomb problem<sup>23</sup>. The periodic images were treated using an optimized Ewald break-up<sup>24</sup> that we applied to the pair action<sup>25</sup>. The explicit treatment of electrons as paths leads to the fermion sign problem, which requires one to introduce the only uncontrolled approximation in this method, the fixed node approximation<sup>26,27</sup>. We use the nodes from the free-particle density matrix and from a variational density matrix<sup>28</sup>. Besides this approximation, all correlation effects are included in PIMC, which for example leads an exact treatment of the isolated helium atom.

The DFT-MD simulations were performed with either the CPMD code<sup>29</sup> using local Troullier-Martins norm-conserving pseudopotentials<sup>30</sup> or with the Vienna ab initio simulation package<sup>31</sup> using the projector augmented-wave method<sup>32</sup>. The nuclei were propagated using Born-Oppenheimer molecular dynamics with forces derived from either the electronic ground state or by including thermally excited electronic states when needed. Exchange-correlation effects were described by the Perdew-Burke-Ernzerhof generalized gradient approximation<sup>33</sup>. The electronic wavefunctions were expanded in a plane-wave basis with energy cut-off of 30-50 Hartrees. Most simulations were performed with  $N=64$  using  $\Gamma$  point sampling of the Brillouin zone. An analysis of finite size effect is presented in the following section.

## III. EQUATION OF STATE

An analysis of finite size dependence of the EOS results is important since all simulation are performed with a finite number of particles in periodic boundary conditions. Figure 1 gives two examples for the finite size analysis that we have performed at various  $(T, \rho)$  conditions. At 10 000 K and  $r_s = 2.4$ , helium can be characterized as a hard-sphere fluid. The artificial periodicity of the nuclei dominates the finite size errors. Simulations with  $N = 64$  atoms are sufficiently accurate for the purpose of this study. The DFT-MD results also agree surprisingly well with classical Monte Carlo calculation using the Aziz pair potential<sup>34</sup>, which explains why both methods give fairly similar Hugoniot curves as long as electronic excitations are not important<sup>17</sup>.

The upper panel of Fig. 1 shows PIMC results for 125 000 K where a substantial part of the pressure comes from excited electrons. They are still coupled to the motion of the nuclei, which leads to effective screening. In

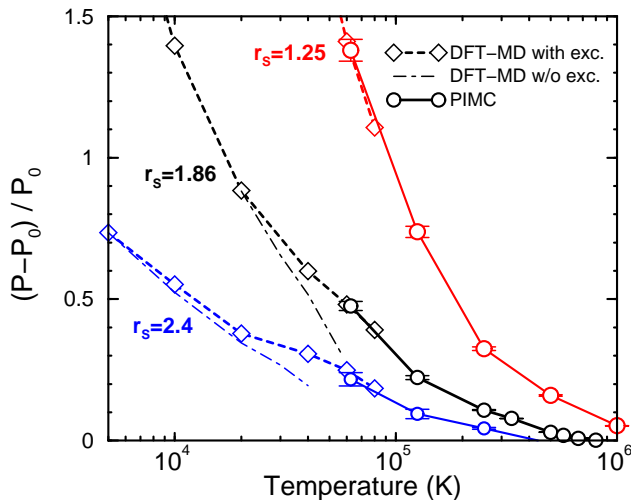


FIG. 2: Comparison of the relative excess pressure derived from PIMC (solid lines) and DFT-MD. The dashed and the dash-dotted lines show results DFT-MD simulation with and without the consideration of thermally excited electronic states, respectively.

consequence, the finite size dependence of the pressure is reduced significantly, and a simulation with  $N = 16$  atoms exhibit a finite size error of only 1% compared with 3% at lower temperature. This is reason why PIMC simulations with 16 atoms already gave a fairly accurate shock Hugoniot curve<sup>17</sup>. However, most PIMC results reported in Tab. I were obtained with 32 atoms and some with 57 atoms. Already 32 atoms lead to well converged pressures unless one is interested at very high temperature above  $10^7$  K where all atoms are ionized and the coupling is very weak. Although the total pressure is dominated by the kinetic term, the excess pressure shows an increased finite size dependence that requires simulation with 57 atoms in some cases. In general, the weak-coupling limit is difficult to study with finite-size simulations<sup>35</sup>. Also at very high density beyond the range considered here, electrons approach the limit of an ideal Fermi gas and form a rigid background. The remaining Coulombic subsystem of ions is expected to require simulations with several hundreds of particles<sup>36</sup>. In this regard, the electronic screening makes our simulations affordable.

Figure 2 compares the pressures obtained from PIMC and DFT-MD simulations for several density. Above 20000 K, excited electronic state become important. Both first-principles method are in very good agreement, which is foundation for the coherent EOS reported in this paper. Reasonably good agreement between PIMC and DFT-MD was reported for hydrogen earlier<sup>37</sup>. Figure 2 is a stringent test because it compares only the pressure contributions that result from the particle interactions. When one removes the ideal gas contributions,  $P_0$ , has one a bit of a choice for the corresponding noninteracting system. At very high temperature, one wants to compare with an ideal Fermi gas of electrons and nuclei. At

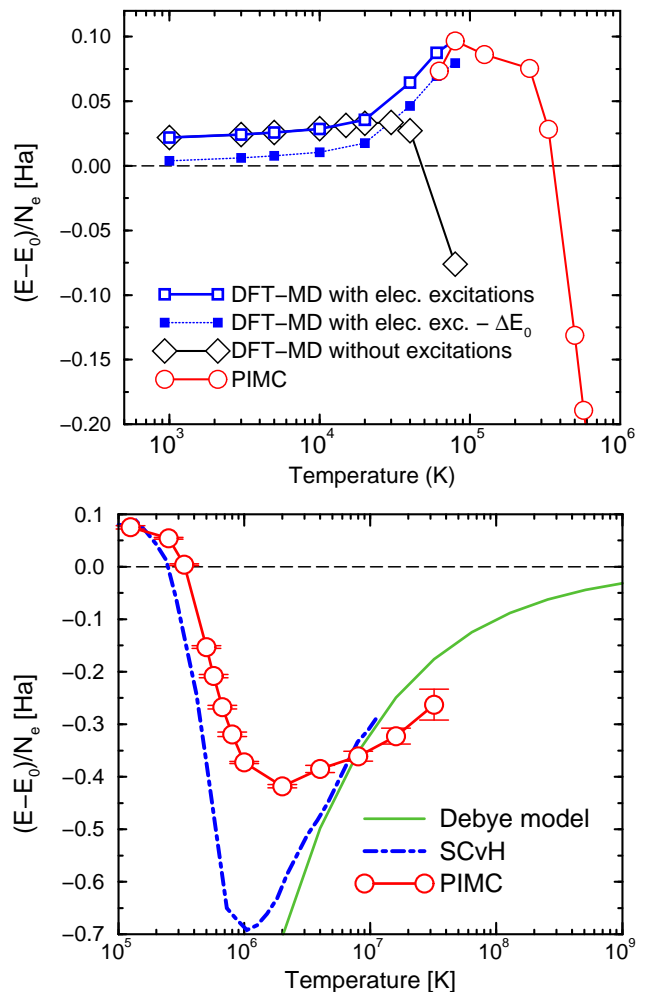


FIG. 3: Excess internal energy per electron relative to the ideal plasma model at a density of  $r_s=1.86$ . The circles show PIMC results. In the upper panel, the open squares and diamonds show DFT-MD results with and without thermal population of excited electronic states; respectively. The filled squares shows DFT-MD results corrected by constant shift corresponding to the DFT error of the isolated helium atom. In lower panel, PIMC results are compared with the Debye model.

low temperature, however, one prefers comparing with a gas of noninteracting atoms. To combine these to limiting cases, we construct a simple chemical model that includes neutral atoms,  $\text{He}^+$  and  $\text{He}^{2+}$  ions as well as free electrons. The ionization state is derived from the Saha equilibrium using the following binding energies,  $E_{\text{He}} = -79.0$  eV,  $E_{\text{He}^+} = -54.4$  eV. Besides the binding energies, no other interaction are considered.

This approach smoothly connects the low- and high-temperature limits. However for the correct interpretation of the presented graphs, it should be pointed out that the pressures and energies of the ideal model depend on the Saha ionization equilibrium. If the ideal system exhibits a higher degree of ionization than the

TABLE I: EOS table with pressures, internal and free energies per electron derived from (a) DFT-MD with 64 atoms (a uniform  $\Delta E/N_e = -0.4909$  Ha correction was added to account for missing DFT correlation energy in the helium atom), PIMC with (b) 32 atoms, (c) PIMC with 57 atoms, and (d) Debye-Hückel limiting law. The numbers in brackets indicate the statistical uncertainties of the DFT-MD and PIMC simulations for the corresponding number trailing digits.

$r_s$	$T$ (K)	$P$ (GPa)	$E/N_e$ (Ha)	$F/N_e$ (Ha)
2.4 <sup>a</sup>	500	1.420(10)	-1.449873(7)	-1.4554
2.4 <sup>a</sup>	1000	2.045(14)	-1.448401(10)	-1.46135
2.4 <sup>a</sup>	3000	4.69(3)	-1.44273(3)	-1.49126
2.4 <sup>a</sup>	5000	6.98(4)	-1.43727(3)	-1.52534
2.4 <sup>a</sup>	10000	12.49(4)	-1.42395(5)	-1.61873
2.4 <sup>a</sup>	20000	22.19(8)	-1.39427(12)	-1.82386
2.4 <sup>a</sup>	40000	43.37(11)	-1.2997(2)	-2.28643
2.4 <sup>a</sup>	60000	68.27(10)	-1.1748(2)	-2.80627
2.4 <sup>a</sup>	80000	96.93(12)	-1.02525(7)	-3.37236
2.4 <sup>b</sup>	125000	172.3(6)	-0.6667(17)	-4.77369
2.4 <sup>b</sup>	250000	445.7(6)	0.477(2)	-9.31702
2.4 <sup>b</sup>	333333	651.4(9)	1.237(3)	-12.6707
2.4 <sup>b</sup>	500000	1067.7(1.0)	2.634(3)	-19.922
2.4 <sup>b</sup>	571428	1249.9(9)	3.216(3)	-23.1952
2.4 <sup>b</sup>	666667	1484.2(5)	3.9507(16)	-27.6612
2.4 <sup>b</sup>	800000	1815.5(1.2)	4.972(4)	-34.0708
2.4 <sup>b</sup>	1×10 <sup>6</sup>	2308.4(7)	6.470(2)	-43.9954
2.4 <sup>b</sup>	2×10 <sup>6</sup>	4745.2(8)	13.754(2)	-97.4249
2.4 <sup>b</sup>	4×10 <sup>6</sup>	9587.6(1.2)	28.102(4)	-213.949
2.4 <sup>d</sup>	8×10 <sup>6</sup>	19253	56.72	-466.803
2.4 <sup>d</sup>	16×10 <sup>6</sup>	38577	113.80	-1013.36
2.4 <sup>d</sup>	32×10 <sup>6</sup>	77205	227.87	-2184.48
2.4 <sup>d</sup>	64×10 <sup>6</sup>	154445	455.92	-4683.43
2.4 <sup>d</sup>	128×10 <sup>6</sup>	308916	911.97	-10002.6
2.4 <sup>d</sup>	256×10 <sup>6</sup>	617849	1824.04	-21267.5
2.4 <sup>d</sup>	512×10 <sup>6</sup>	1235711	3648.14	-45052.4
2.4 <sup>d</sup>	1024×10 <sup>6</sup>	2471430	7296.32	-95193.5
2.4 <sup>d</sup>	2048×10 <sup>6</sup>	4942866	14592.67	-200489

simulation results, then this alone can lead to negative excess pressures and energies, which one would normally attribute exclusively to the interaction of free electrons and ions. This effect becomes clear in Fig. 3 where even the DFT-MD results without excited electrons exhibit a negative excess internal energy at 80 000 K.

Figure 3 exhibits the missing correlation energies in DFT GGA, which underestimates the binding energy in the atom by  $\Delta E_0=0.98$  eV. This is the main reason for the disagreement with the ideal plasma model in the low-temperature limit (1.20 eV/atom), while internal energy increase due to the compression to  $r_s = 1.86$  amounts only to 0.22 eV/atom. To correct for missing correlation energy, we applied a uniform correction of  $-\Delta E_0$  to all DFT results discussed later. We may assume that the correction to DFT depends only weakly on temperature and density. To determine its precise amount more accurately is difficult and goes beyond the scope of this article.

Despite this DFT insufficiency, one finds reasonably good agreement in the internal energies reported by

TABLE II: Table I continued.

$r_s$	$T$ (K)	$P$ (GPa)	$E/N_e$ (Ha)	$F/N_e$ (Ha)
2.2 <sup>a</sup>	500	2.74(2)	-1.449495(13)	-1.45451
2.2 <sup>a</sup>	1000	3.77(3)	-1.44787(2)	-1.4601
2.2 <sup>a</sup>	3000	7.59(3)	-1.44186(2)	-1.48855
2.2 <sup>a</sup>	5000	10.81(6)	-1.43615(3)	-1.5214
2.2 <sup>a</sup>	10000	18.23(7)	-1.42256(5)	-1.61205
2.2 <sup>a</sup>	20000	31.39(7)	-1.39256(9)	-1.812
2.2 <sup>a</sup>	40000	59.54(13)	-1.30036(19)	-2.2635
2.2 <sup>a</sup>	60000	92.10(11)	-1.17937(16)	-2.77064
2.2 <sup>a</sup>	80000	129.52(10)	-1.03399(12)	-3.32222
2.2 <sup>b</sup>	125000	223.9(7)	-0.6962(16)	-4.68439
2.2 <sup>b</sup>	250000	569.6(7)	0.3971(16)	-9.08923
2.2 <sup>b</sup>	500000	1371.3(6)	2.5403(14)	-19.3777
2.2 <sup>b</sup>	1×10 <sup>6</sup>	2981.1(7)	6.3896(17)	-42.807
2.2 <sup>b</sup>	2×10 <sup>6</sup>	6148.3(8)	13.694(2)	-95
2.2 <sup>b</sup>	4×10 <sup>6</sup>	12438.6(1.7)	28.059(4)	-209.039
2.2 <sup>d</sup>	8×10 <sup>6</sup>	24982	56.67	-456.924
2.2 <sup>d</sup>	16×10 <sup>6</sup>	50075	113.77	-993.605
2.2 <sup>d</sup>	32×10 <sup>6</sup>	100227	227.85	-2144.93
2.2 <sup>d</sup>	64×10 <sup>6</sup>	200508	455.91	-4604.15
2.2 <sup>d</sup>	128×10 <sup>6</sup>	401053	911.96	-9843.99
2.2 <sup>d</sup>	256×10 <sup>6</sup>	802134	1824.03	-20951.2
2.2 <sup>d</sup>	512×10 <sup>6</sup>	1604287	3648.13	-44420.5
2.2 <sup>d</sup>	1024×10 <sup>6</sup>	3208587	7296.31	-93928.4
2.2 <sup>d</sup>	2048×10 <sup>6</sup>	6417184	14592.66	-197960
2 <sup>a</sup>	500	6.101(13)	-1.448584(6)	-1.45297
2 <sup>a</sup>	1000	7.59(2)	-1.446835(11)	-1.45806
2 <sup>a</sup>	3000	13.57(5)	-1.44022(3)	-1.48466
2 <sup>a</sup>	5000	18.07(7)	-1.43433(4)	-1.51606
2 <sup>a</sup>	10000	28.62(11)	-1.42013(8)	-1.60363
2 <sup>a</sup>	20000	47.02(12)	-1.38968(11)	-1.79771
2 <sup>a</sup>	40000	84.72(12)	-1.30039(15)	-2.23673
2 <sup>a</sup>	60000	128.66(14)	-1.18357(12)	-2.72986
2 <sup>a</sup>	80000	178.84(19)	-1.0433(2)	-3.26574
2 <sup>b</sup>	125000	297.4(7)	-0.7291(12)	-4.58614
2 <sup>b</sup>	250000	745.9(7)	0.3112(13)	-8.84403
2 <sup>b</sup>	500000	1800.9(8)	2.4269(14)	-18.7895
2 <sup>b</sup>	1×10 <sup>6</sup>	3941.2(1.0)	6.2898(17)	-41.5111
2 <sup>b</sup>	2×10 <sup>6</sup>	8163.1(1.5)	13.621(3)	-92.3417
2 <sup>b</sup>	4×10 <sup>6</sup>	16544(2)	28.009(4)	-203.653
2 <sup>d</sup>	8×10 <sup>6</sup>	33228	56.61	-446.089
2 <sup>d</sup>	16×10 <sup>6</sup>	66633	113.73	-971.926
2 <sup>d</sup>	32×10 <sup>6</sup>	133390	227.82	-2101.53
2 <sup>d</sup>	64×10 <sup>6</sup>	266868	455.88	-4517.11
2 <sup>d</sup>	128×10 <sup>6</sup>	533797	911.95	-9669.7
2 <sup>d</sup>	256×10 <sup>6</sup>	1067636	1824.02	-20604.1
2 <sup>d</sup>	512×10 <sup>6</sup>	2135303	3648.12	-43727.2
2 <sup>d</sup>	1024×10 <sup>6</sup>	4270628	7296.31	-92540.1
2 <sup>d</sup>	2048×10 <sup>6</sup>	8541271	14592.66	-195186

PIMC and DFT-MD. Figure 3 shows that both methods report very similar increases in the energy resulting from thermal excitations of electrons, which is the basis for constructing one EOS table.

In order to explore the agreement between PIMC and DFT-MD in more detail we resort to pressure calculations for a single configuration of nuclei that we have obtain from DFT-MD with 57 atoms at 80 000 K. The

TABLE III: Table II continued.

$r_s$	$T$ (K)	$P$ (GPa)	$E/N_e$ (Ha)	$F/N_e$ (Ha)
1.86 <sup>a</sup>	1000	13.55(3)	-1.445347(12)	-1.45574
1.86 <sup>a</sup>	3000	21.50(8)	-1.43837(4)	-1.48081
1.86 <sup>a</sup>	5000	28.04(9)	-1.43196(4)	-1.51097
1.86 <sup>a</sup>	10000	41.40(10)	-1.41740(6)	-1.59608
1.86 <sup>a</sup>	20000	65.16(13)	-1.38638(9)	-1.7856
1.86 <sup>a</sup>	40000	112.98(18)	-1.29844(18)	-2.2149
1.86 <sup>a</sup>	60000	167.7(2)	-1.1854(2)	-2.69739
1.86 <sup>a</sup>	80000	229.42(15)	-1.04980(12)	-3.22147
1.86 <sup>c</sup>	125000	378(2)	-0.743(3)	-4.51072
1.86 <sup>b</sup>	250000	918.6(1.3)	0.2491(18)	-8.65932
1.86 <sup>b</sup>	333333	1340.7(1.3)	0.9607(18)	-11.7193
1.86 <sup>b</sup>	500000	2214.5(1.7)	2.336(2)	-18.3468
1.86 <sup>b</sup>	571428	2595(2)	2.910(3)	-21.3458
1.86 <sup>b</sup>	666667	3104(3)	3.661(4)	-25.4472
1.86 <sup>b</sup>	800000	3818(3)	4.699(4)	-31.3521
1.86 <sup>b</sup>	$1 \times 10^6$	4876.7(1.5)	6.212(2)	-40.5306
1.86 <sup>b</sup>	$2 \times 10^6$	10128(3)	13.559(3)	-90.3193
1.86 <sup>b</sup>	$4 \times 10^6$	20550(5)	27.959(7)	-199.554
1.86 <sup>b</sup>	$8 \times 10^6$	41316(7)	56.543(9)	-437.845
1.86 <sup>d</sup>	$16 \times 10^6$	82822	113.69	-955.409
1.86 <sup>d</sup>	$32 \times 10^6$	165822	227.79	-2068.45
1.86 <sup>d</sup>	$64 \times 10^6$	331768	455.87	-4450.87
1.86 <sup>d</sup>	$128 \times 10^6$	663625	911.93	-9537.1
1.86 <sup>d</sup>	$256 \times 10^6$	1327312	1824.01	-20338.8
1.86 <sup>d</sup>	$512 \times 10^6$	2654668	3648.12	-43196.4
1.86 <sup>d</sup>	$1024 \times 10^6$	5309366	7296.30	-91478.5
1.86 <sup>d</sup>	$2048 \times 10^6$	10618754	14592.66	-193062
1.75 <sup>a</sup>	1000	22.14(4)	-1.443419(13)	-1.45302
1.75 <sup>a</sup>	3000	32.35(11)	-1.43604(4)	-1.47673
1.75 <sup>a</sup>	5000	40.66(13)	-1.42933(5)	-1.50576
1.75 <sup>a</sup>	10000	57.60(13)	-1.41415(6)	-1.58867
1.75 <sup>a</sup>	20000	87.06(17)	-1.38263(11)	-1.77422
1.75 <sup>a</sup>	40000	144.6(3)	-1.2961(3)	-2.19531
1.75 <sup>a</sup>	60000	210.43(19)	-1.18602(16)	-2.66885
1.75 <sup>a</sup>	80000	284.6(3)	-1.05398(16)	-3.18308
1.75 <sup>b</sup>	125000	454.4(1.0)	-0.7647(12)	-4.44653
1.75 <sup>b</sup>	250000	1098.0(1.1)	0.2015(13)	-8.50508
1.75 <sup>b</sup>	500000	2639.1(1.6)	2.2626(17)	-17.9781
1.75 <sup>b</sup>	$1 \times 10^6$	5831.7(2.0)	6.143(2)	-39.7109
1.75 <sup>b</sup>	$2 \times 10^6$	12139(2)	13.503(3)	-88.6228
1.75 <sup>b</sup>	$4 \times 10^6$	24656(3)	27.915(4)	-196.115
1.75 <sup>b</sup>	$8 \times 10^6$	49587(8)	56.501(10)	-430.926
1.75 <sup>d</sup>	$16 \times 10^6$	99420	113.65	-941.531
1.75 <sup>d</sup>	$32 \times 10^6$	199083	227.76	-2040.64
1.75 <sup>d</sup>	$64 \times 10^6$	398335	455.85	-4395.24
1.75 <sup>d</sup>	$128 \times 10^6$	796789	911.92	-9425.79
1.75 <sup>d</sup>	$256 \times 10^6$	1593662	1824.00	-20115.4
1.75 <sup>d</sup>	$512 \times 10^6$	3187384	3648.11	-42749
1.75 <sup>d</sup>	$1024 \times 10^6$	6374809	7296.30	-90584.7
1.75 <sup>d</sup>	$2048 \times 10^6$	12749648	14592.65	-191274

nuclear coordinates are the  $r_s = 1.86$  snapshot are given in Tab. A in the appendix. For this fixed configuration of nuclei, we now compare the instantaneous pressure as a function of electronic temperature. The fact that the nuclei are now classical rather being represented by paths in PIMC has a negligible effect on the pressure for the

TABLE IV: Table III continued.

$r_s$	$T$ (K)	$P$ (GPa)	$E/N_e$ (Ha)	$F/N_e$ (Ha)
1.5 <sup>a</sup>	1000	73.92(10)	-1.43440(3)	-1.44135
1.5 <sup>a</sup>	2000	84.42(12)	-1.42977(4)	-1.45018
1.5 <sup>a</sup>	3000	92.66(12)	-1.42576(4)	-1.46128
1.5 <sup>a</sup>	5000	107.7(2)	-1.41813(7)	-1.48725
1.5 <sup>a</sup>	10000	137.9(3)	-1.40115(11)	-1.56358
1.5 <sup>a</sup>	20000	189.4(4)	-1.36731(18)	-1.73814
1.5 <sup>a</sup>	40000	285.0(4)	-1.2819(2)	-2.13878
1.5 <sup>a</sup>	60000	387.4(4)	-1.1802(2)	-2.58963
1.5 <sup>a</sup>	80000	505.3(3)	-1.05690(13)	-3.07884
1.5 <sup>b</sup>	125000	770(2)	-0.7880(16)	-4.27821
1.5 <sup>b</sup>	250000	1737.1(1.6)	0.0907(12)	-8.11696
1.5 <sup>b</sup>	500000	4114.7(1.6)	2.0709(12)	-17.0558
1.5 <sup>b</sup>	$1 \times 10^6$	9147.6(1.6)	5.9425(12)	-37.6523
1.5 <sup>b</sup>	$2 \times 10^6$	19175(2)	13.3390(15)	-84.3488
1.5 <sup>b</sup>	$4 \times 10^6$	39062(5)	27.782(4)	-187.433
1.5 <sup>b</sup>	$8 \times 10^6$	78690(10)	56.411(8)	-413.442
1.5 <sup>c</sup>	$16 \times 10^6$	157860(7)	113.544(5)	-906.451
1.5 <sup>d</sup>	$32 \times 10^6$	316058	227.68	-1970.31
1.5 <sup>d</sup>	$64 \times 10^6$	632486	455.79	-4254.46
1.5 <sup>d</sup>	$128 \times 10^6$	1265232	911.88	-9143.99
1.5 <sup>d</sup>	$256 \times 10^6$	2530649	1823.97	-19550.3
1.5 <sup>d</sup>	$512 \times 10^6$	5061428	3648.09	-41618.1
1.5 <sup>d</sup>	$1024 \times 10^6$	10122947	7296.28	-88324.9
1.5 <sup>d</sup>	$2048 \times 10^6$	20245959	14592.64	-186751
1.25 <sup>a</sup>	3000	331.6(3)	-1.39652(6)	-1.42554
1.25 <sup>a</sup>	5000	360.1(5)	-1.38761(12)	-1.44742
1.25 <sup>a</sup>	10000	418.6(4)	-1.36798(8)	-1.51449
1.25 <sup>a</sup>	20000	515.4(8)	-1.3306(3)	-1.67468
1.25 <sup>a</sup>	40000	683.9(5)	-1.24615(18)	-2.05136
1.25 <sup>a</sup>	60000	865.2(7)	-1.1504(2)	-2.47506
1.25 <sup>a</sup>	80000	1063.2(1.0)	-1.0378(3)	-2.93438
1.25 <sup>a</sup>	125000	1565.4(1.5)	-0.7817(4)	-4.05965
1.25 <sup>b</sup>	250000	3074(3)	-0.0069(11)	-7.65192
1.25 <sup>b</sup>	500000	6999(4)	1.8502(15)	-15.9783
1.25 <sup>b</sup>	$1 \times 10^6$	15578(3)	5.6796(11)	-35.2469
1.25 <sup>b</sup>	$2 \times 10^6$	32897(7)	13.107(3)	-79.3259
1.25 <sup>b</sup>	$4 \times 10^6$	67243(80)	27.58(3)	-177.186
1.25 <sup>b</sup>	$8 \times 10^6$	135808(19)	56.263(8)	-392.772
1.25 <sup>b</sup>	$16 \times 10^6$	272614(30)	113.381(13)	-864.979
1.25 <sup>d</sup>	$32 \times 10^6$	545908	227.54	-1887.16
1.25 <sup>d</sup>	$64 \times 10^6$	1092767	455.69	-4087.74
1.25 <sup>d</sup>	$128 \times 10^6$	2186203	911.81	-8810.14
1.25 <sup>d</sup>	$256 \times 10^6$	4372877	1823.92	-18883.5
1.25 <sup>d</sup>	$512 \times 10^6$	8746088	3648.06	-40286
1.25 <sup>d</sup>	$1024 \times 10^6$	17492411	7296.26	-85659.8
1.25 <sup>d</sup>	$2048 \times 10^6$	34984988	14592.63	-181419

temperatures under consideration. In both methods, the instantaneous pressure is a well-defined quantity derived from the virial theorem. In DFT, one uses the diagonal elements of the stress tensor<sup>38</sup>, while in PIMC one derives the pressure directly from the kinetic,  $\langle \mathcal{K} \rangle$ , and potential,  $\langle \mathcal{V} \rangle$ , energy,

$$3PV = 2 \langle \mathcal{K} \rangle + \langle \mathcal{V} \rangle, \quad (1)$$

where  $V$  is the volume of the simulation cell. DFT is primarily a groundstate method that use an exchange func-

TABLE V: Table IV continued.

$r_s$	$T$ (K)	$P$ (GPa)	$E/N_e$ (Ha)	$F/N_e$ (Ha)
$1^a$	5000	1560.1(5)	-1.29739(8)	-1.34504
$1^a$	10000	1681.8(7)	-1.27401(12)	-1.40096
$1^a$	20000	1878.6(1.0)	-1.2313(2)	-1.5439
$1^a$	40000	2217.0(1.8)	-1.1449(3)	-1.88916
$1^a$	62500	2608.7(1.8)	-1.0456(3)	-2.33028
$1^a$	80000	2941(2)	-0.9554(4)	-2.7022
$1^a$	125000	3890(2)	-0.7276(4)	-3.73996
$1^b$	250000	6640(6)	-0.0380(12)	-7.04803
$1^b$	333333	8780(6)	0.4717(12)	-9.46272
$1^b$	500000	13687(5)	1.6229(11)	-14.6687
$1^b$	571428	15920(5)	2.1410(11)	-17.0286
$1^b$	666667	18969(5)	2.8429(11)	-20.2721
$1^b$	800000	23334(5)	3.8385(12)	-24.9776
$1^b$	$1 \times 10^6$	29972(5)	5.3367(12)	-32.3609
$1^b$	$2 \times 10^6$	63676(11)	12.775(2)	-73.2177
$1^b$	$4 \times 10^6$	130941(12)	27.326(3)	-164.669
$1^b$	$8 \times 10^6$	264847(50)	56.052(10)	-367.49
$1^c$	$16 \times 10^6$	532209(20)	113.270(5)	-814.18
$1^c$	$32 \times 10^6$	1066140(60)	227.350(14)	-1785.39
$1^d$	$64 \times 10^6$	2133644	455.50	-3884.05
$1^d$	$128 \times 10^6$	4269457	911.68	-8402.62
$1^d$	$256 \times 10^6$	8540444	1823.83	-18068.8
$1^d$	$512 \times 10^6$	17081968	3647.99	-38656.7
$1^d$	$1024 \times 10^6$	34164699	7296.21	-82400.7
$1^d$	$2048 \times 10^6$	68329938	14592.59	-174902

tional that was derived at  $T=0$ . It allows, however, to include electronic excitations using a thermal population of excited single-particle states. On the other hand, PIMC is a finite temperature quantum simulation method that treats the electrons as interacting particles. The only approximation comes from the fermion nodes.

Figure 4 compares the instantaneous pressures from both methods. At intermediate temperatures, there is a large interval where both methods agree. DFT pressures appear to be fairly accurate. For the level of accuracy needed for this study we could not detect any insufficiency resulting from the groundstate exchange correlation functional nor from inaccurate thermal excitations resulting from an underestimated bandgap. However, the DFT eventually become prohibitively expensive at higher temperature. Some of the points at  $r_s = 2.4$  required up to 100 bands per atom, and that is one reason why we only used a single configuration. The other comes from path integrals. PIMC simulations with 123 atoms shown in Fig. 1 represent about the limit one can study with currently available computers. If one wants to repeat the calculations at lower temperature where the paths are longer, or using the more expensive variational nodes, one quickly exceeds existing limits in processing power.

Figure 4 also reveals inaccuracies in the PIMC computation that are caused by approximations in the trial density matrix. PIMC with free-particle nodes predict pressures that are too high when the electrons settle into the ground state ( $T \leq 40\,000$  K for  $r_s=1.86$  as shown in Fig. 2). This effect has already been reported for hy-

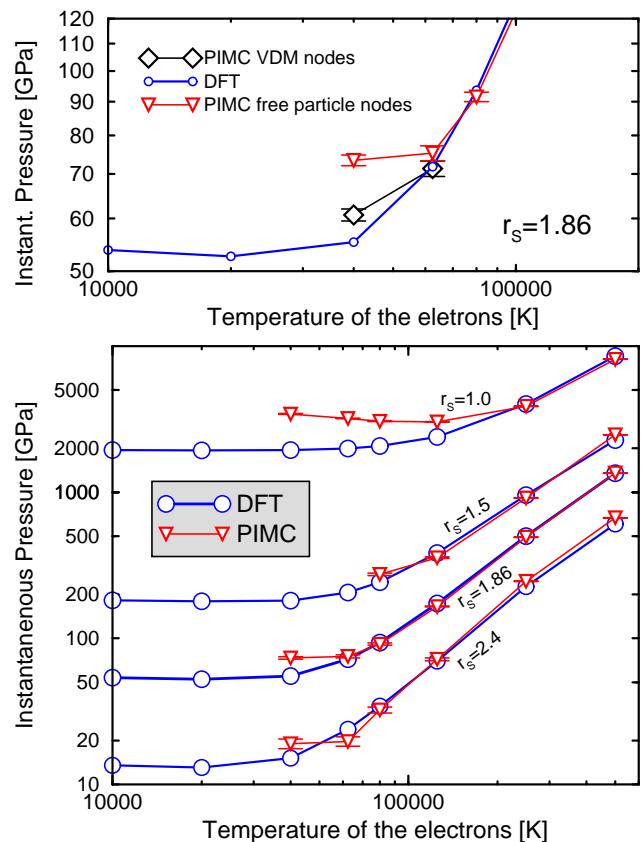


FIG. 4: Comparison of the instantaneous pressure for a fixed configuration of nuclei derived from PIMC and DFT with thermally populated states. The upper panel included results from PIMC with variational nodes. The lower panel compares PIMC results with free-particle nodes for different densities. (The ideal gas contributions from the nuclei are not included.)

drogen<sup>14</sup>. In the variational density matrix approach<sup>28</sup> one allows the trial density matrix to adjust to the positions of the nuclei, which corrects most of the pressure error as can be seen in upper panel of Fig. 4. However, the variational approach was derived to study finite temperature problems. It does not describe the electronic ground state as well as DFT.

For the purpose of construction one EOS table for helium, we use DFT-MD results with electronic excitation up to 80 000 K for  $r_s \geq 1.5$  and results up to 125 000 K for  $r_s = 1.25$  and 1.0. For all higher  $T$ , we use PIMC simulations, which become more and more efficient at higher  $T$  because the length of the paths is inversely proportional to temperature.

It should be noted that the discussed validity range of different trial density matrices depends very much on the material under consideration. The temperature where we switch from PIMC to DFT-MD reflects the degree of thermal electronic excitations as well as some dependence of the approximations made in both methods. The density dependence of the switching temperature would typically be estimated by comparing the temperature to

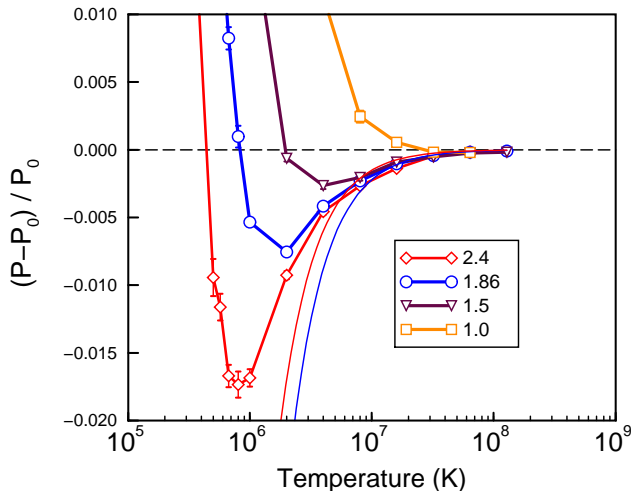


FIG. 5: The relative excess pressure derived from PIMC (thick lines with symbols) is compared with Debye-Hückel plasma model (thin lines) for different values of  $r_s$  given in the legend. The ideal pressure,  $P_0$ , is derived Saha model of noninteracting helium species (see text).

the Fermi energy of an ideal gas of electrons. However, to incorporate band structure effects of dense helium, we found it more appropriate to relate the switching temperature to the DFT band width. Band width and Fermi energy are identical in the systems of noninteracting particles. For the purpose of this study, we found it appropriate to switch from PIMC to DFT-MD for temperatures corresponding to less than one third of the helium band width.

We performed PIMC simulations up to  $1.28 \times 10^8$  K covering a large temperature interval of two orders of magnitude. The excess internal energies and pressures in Figs. 2, 3, and 5 are positive at lower temperatures reflecting electronic excitations but then change sign due to interactions of ions and free electrons. At very high temperature when helium is fully ionized, the system can be described by the Debye plasma model<sup>39</sup>. The Debye model is based on a self-consistent solution of the Poisson equation for a system of screened charges. The excess contribution to the free energy, internal energy, entropy per particle, and pressure are given by,

$$\frac{F}{N_p} = \frac{\Xi}{12}, \quad \frac{E}{N_p} = \frac{\Xi}{8}, \quad \frac{S}{N_p} = \frac{\Xi}{24}, \quad P = \frac{\Xi}{24V}, \quad (2)$$

$$\Xi = -k_B T V \frac{\kappa^3}{\pi}, \quad \kappa^2 = \frac{4\pi}{k_B T} \sum_i Z_i^2 \frac{N_i}{V}, \quad (3)$$

where  $\kappa = 1/r_d$  is the inverse of Debye radius,  $r_d$ , in a collection of  $N_i$  particles of charge  $Z_i$  in volume  $V$  where  $N_p = \sum_i N_i$ . Figure 5 demonstrates very good agreement with the Debye model at high temperature. The Debye model fails at lower temperatures where it predicts unphysically low pressures. Under these conditions the screening approximation fails because there are too few

particles in the Debye sphere. The number of particles in the Debye sphere is proportional to,

$$(r_d/r_s)^3 \sim (T r_s)^{3/2}, \quad (4)$$

which means that the Debye model becomes increasingly accurate for high  $T$  and large  $r_s$ . This is exactly what is observed in Fig. 5. For higher densities, PIMC and Debye predictions converge only at higher temperatures.

The size of the Debye sphere increases with temperature and will eventually exceed the size of any simulation cell. This occurs when the coupling the particles become very weak. With increasing temperature, the Coulomb energy decreases while the kinetic energy increases linearly with  $T$ . To determine the precise amount of the Coulomb energy becomes more and more difficult due to finite size effects. This is the reason why the PIMC simulations do not agree perfectly with the Debye model for the highest temperature shown in the lower panel of Fig. 3. In conclusion, we use the Debye EOS for the highest data in our EOS table. The nonideal pressures reported in Fig. 5 appear to be less sensitive to finite size errors than the internal energy because their volume dependence is relatively weak.

Now we compare our first-principle EOS with chemical free energy models that were developed before first-principles simulation data became available. Winisdoerfer and Chabrier<sup>40</sup> constructed a semianalytical model to study stellar interiors that covers a wide density range including metallization. Their EOS is only available in explicit form in a small temperature interval and a comparison with DFT-MD simulation has already been reported<sup>19</sup>. That is why we focus on the free energy model derived by Saumon, Chabrier, and van Horn (SCvH)<sup>41</sup>. Together with their hydrogen model<sup>42</sup>, their EOS has been used numerous times to model giant planet interiors.

Figure 6 compares the excess pressure from both EOSs for three different temperatures. At a very temperature of  $10^6$  K that are important for stellar interiors, we found fairly good agreement. The deviations between the SCvH model and PIMC simulations are only about 4%.

At an intermediate temperature of 100 000 K, that approximately represent the regime of shock wave experiments, the agreement is less favorable. One finds that the SCvH EOS reports pressures that are about 30% lower than those predicted by PIMC. This is partly due to the fact that the SCvH model follows the Debye model down to too low temperatures (Fig. 3) and that an interpolation scheme between a low and a high-temperature model was used by SCvH that was not thermodynamically consistent (Fig. 13).

The last panel in Fig. 6 is focused on the interiors of giant planets with temperature of the order to 10 000 K. At low density both EOSs agree well, but above  $1.5 \text{ g cm}^{-3}$  deviation begins to increase steadily. At conditions comparable to Jupiter's interior, we find that the SCvH underestimates the pressure by 30%. In a hydrogen-helium mixture of solar composition, this translates into an er-

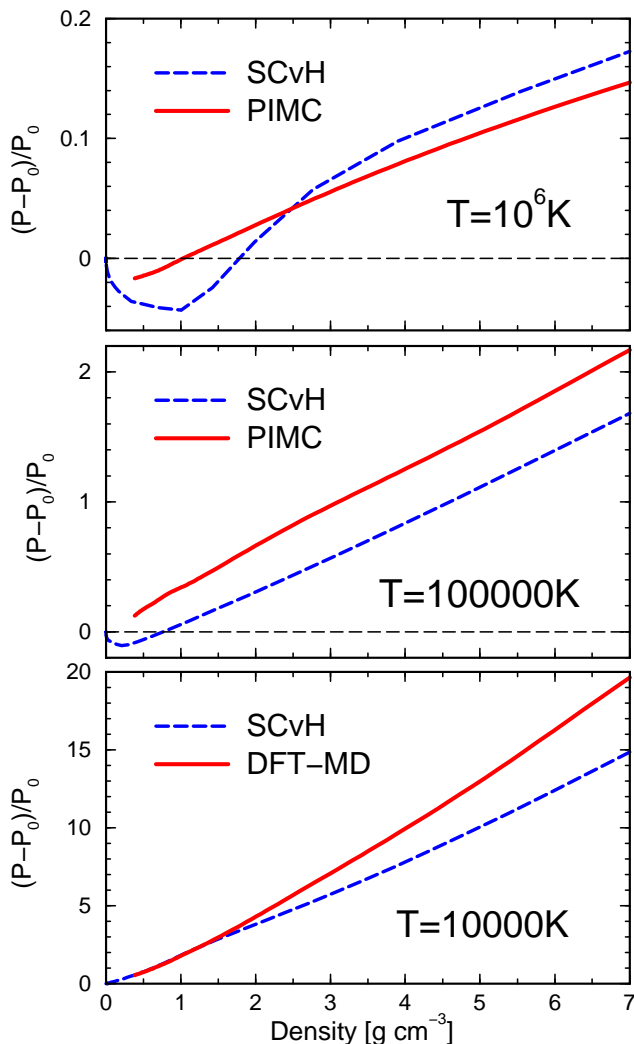


FIG. 6: Comparison of the relative excess pressure reported by first-principles simulations with the SCvH EOS model. The three temperatures shown here are relevant for stellar interiors, the comparison with shock wave experiments, and the interiors of giant planets.

ror in the pressure of about 4%. This is the reason why even the helium EOS is important to estimate the size of Jupiter’s core, which is expected to be only a small fraction of the Jupiter’s total mass.

#### IV. PAIR CORRELATION FUNCTIONS

In this section, we study the structure of the fluid by analyzing correlations between different types of particles. Given the large amount of simulation results, we focus our attention primarily on the temperature dependence and only report results for one density of  $r_s = 1.86$ . The density dependence of the pair correlation functions,  $g(r)$ , has been analyzed in Ref.<sup>37</sup>.

Figure 7 shows how the nuclear pair correlation func-

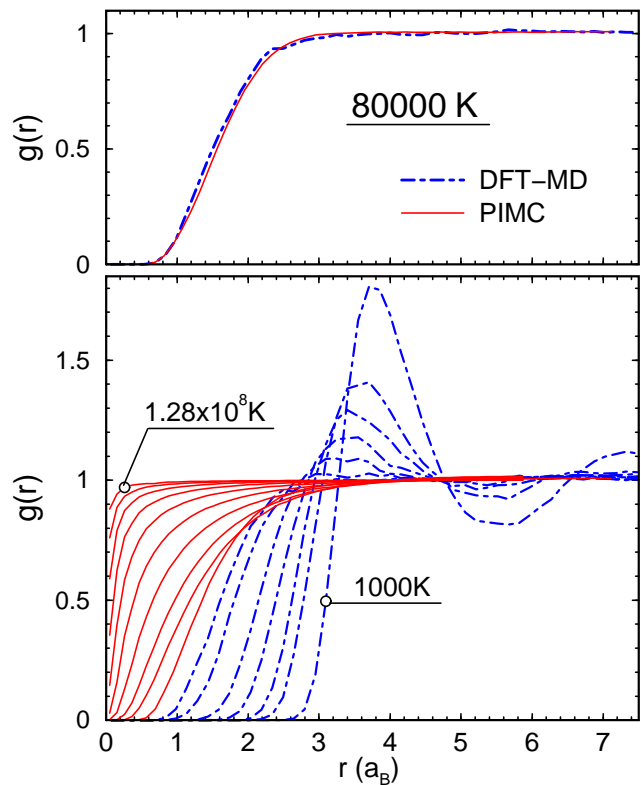


FIG. 7: The nuclear pair correlation functions for  $r_s = 1.86$ . The lower panel shows the following temperatures:  $\{ 128, 64, 32, 16, 8, 4, 2, 1, 0.5, \text{ and } 0.125 \} \times 10^6$  K from PIMC as well as  $\{ 40, 20, 10, 5, 3, \text{ and } 1 \} \times 10^3$  K from DFT-MD.

tions changes over a temperature interval that spans seven orders of magnitude. At low temperature, the  $g(r)$  shows the oscillatory behavior that is typical for a hard-sphere fluid. The atomic interactions are governed by two tightly bound electrons that lead to a strong repulsion at close range due to Pauli exclusion. As long as the density is not too high, this behavior is well-described by the Aziz pair potential<sup>17</sup>.

As temperature increases, two effects change the pair correlation function. The increase in kinetic energy leads to stronger collisions and atoms approach each other more. This is regard, helium is not exactly a hard-sphere fluid because the Aziz pair potential is not perfectly hard. The increase in temperature also damps of the oscillation in the  $g(r)$ .

At 80 000 K, one finds perfect agreement between PIMC and DFT-MD (upper panel in Fig. 7). As the temperature is increased further, changes in nuclear  $g(r)$  function are dominated by electronic excitations and the ionization of atoms. One finds that the strong repulsion at low temperature disappears gradually. As one approaches the Debye-Hückel limit, the fluid behaves like correlated system of screened Coulomb charges.

The peak in the electron-nucleus pair correlation functions in Fig. 8 illustrates that the electrons are bound to the nuclei. At 40 000 K and below, the peak height



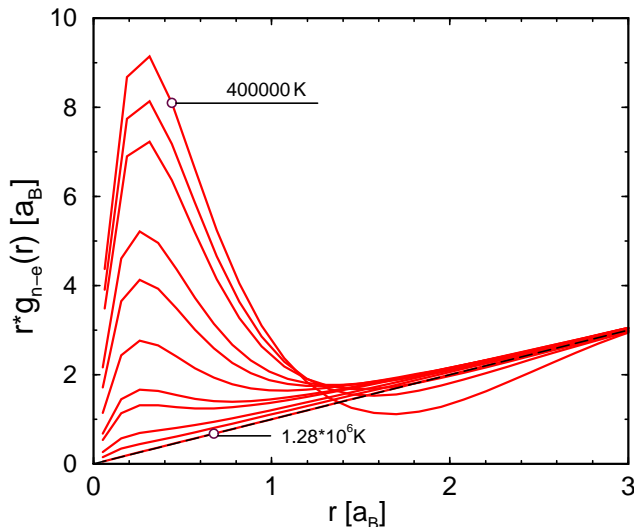


FIG. 8: The electron-nucleus pair correlation functions,  $g(r)$ , from PIMC for  $r_s = 1.86$ . Starting with the highest peak, the following temperatures are plotted:  $\{ 0.04, 0.08, 0.125, 0.25, 0.333, 0.5, 0.8, 1, 2, 4, \text{ and } 128 \} \times 10^6$  K. We plot  $r * g(r)$  on the ordinate so that the peak at small  $r$  illustrates the fraction of electrons in bound states. The decrease in peak height with increasing temperature demonstrates thermal excitation of electrons, which eventually leads the ionization of atoms.

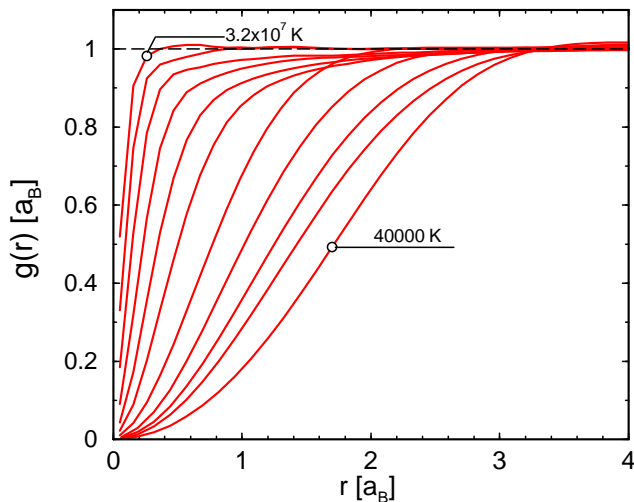


FIG. 9: The electron-electron pair correlation functions for electrons with parallel spins calculated with PIMC for  $r_s = 1.86$ . Starting from the left, the following temperatures are plotted:  $\{ 32, 16, 8, 4, 2, 1, 0.25, 0.125, 0.08, 0.0625, 0.04 \} \times 10^6$  K. With increasing temperature, correlation effects are reduced and the exchange-correlation hole disappears.

is maximal. At higher temperature, electrons get excited and eventually atoms get ionized. The peak height is consequently reduced until, at very high temperature, the motion of electrons and nuclei appears to be uncorrelated.

The correlation of electrons with parallel spins is de-

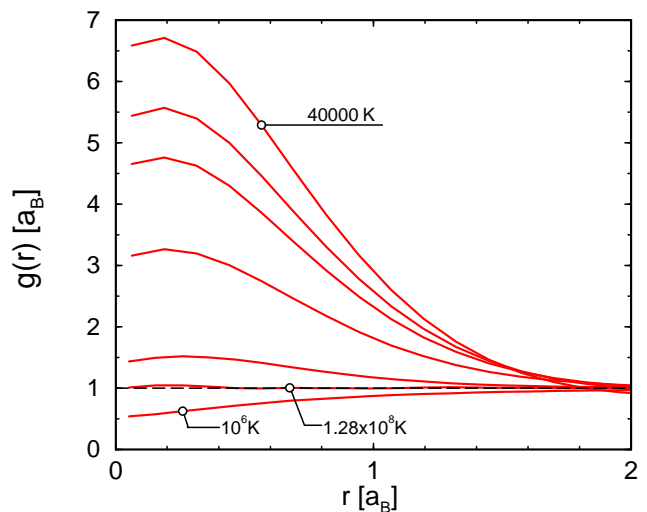


FIG. 10: The electron-electron pair correlation functions for electrons with opposite spins calculated with PIMC for  $r_s = 1.86$ . Starting from the top, the following temperatures are plotted:  $\{ 0.04, 0.0625, 0.08, 0.125, 128, \text{ and } 1 \} \times 10^6$  K. The smallest values are observed for  $10^6$  K.

termined by Pauli exclusion and Coulomb repulsion but is also influenced by the motion of the nuclei at low temperature. Combination of all these effects causes the motion of same-spin electrons to be negatively correlated at small distances. This is typically referred to as the exchange-correlation hole. At high temperatures, kinetic effect reduces the size of this hole but  $g(r)$  always goes to zero for small  $r$  due to Pauli exclusion.

Despite the Coulomb repulsion, the electrons with opposite spins are positively correlated at low temperature, because two electrons with opposite spin are bound in a helium atom. With increasing temperature, the peak in Fig. 10 reduces in height because more and more electrons get ionized. At  $10^6$ , one finds the lowest values for  $g(r \rightarrow 0)$  because the electrons are anti-correlated due to the Coulomb repulsion. If the temperature is increased further kinetic effects dominate over the Coulomb repulsion and  $g(r \rightarrow 0)$  again increases and will eventually approaches 1 at high temperature.

## V. ENTROPY CALCULATIONS

Convection in the interior of planets determines that the temperature-pressure profile is adiabatic. In consequence, the planetary interiors is fully determined by the conditions on the surface and the EOS. This makes the calculation of adiabats important. However, neither Monte Carlo nor molecular dynamics methods can directly compute entropies because both techniques save orders of magnitude in computer time by generating a only representative sample of configurations. Without this gain many-body simulations would be impossible and in consequence, entropies that are measure of the

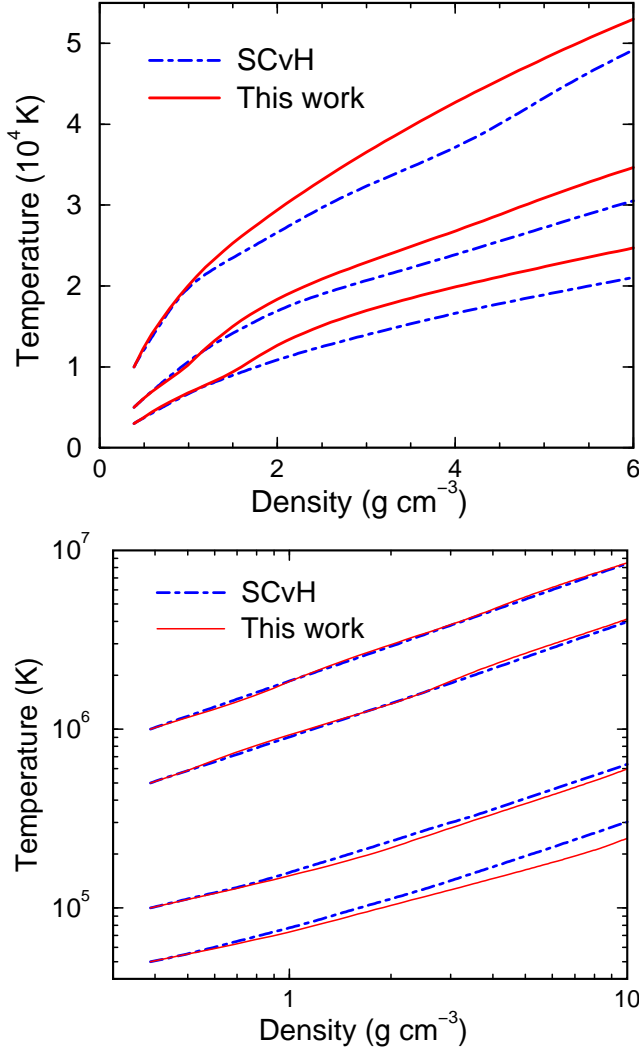


FIG. 11: Comparison in temperature-density space of adiabats from first-principles simulations (this work) and the SCvH EOS model.

total available phase space are not accessible directly.

Typically one derives the entropy by thermodynamic integration from a known reference state. However, for the planetary interiors, the absolute value of the entropy is not important as long as one is able to construct  $(T, P)$  curve of constant entropy. This can be done using the pressure and the internal energy from first-principles simulations at different  $(T, V)$  conditions. Using Maxwell's relations, one finds,

$$\left. \frac{\partial T}{\partial V} \right|_S = - \frac{\left. \frac{\partial S}{\partial V} \right|_T}{\left. \frac{\partial S}{\partial T} \right|_V} = -T \frac{\left. \frac{\partial P}{\partial T} \right|_V}{\left. \frac{\partial E}{\partial T} \right|_V}. \quad (5)$$

By solving this ordinary differential equation,  $(V, T)$ -adiabats can be constructed as long as a sufficiently dense mesh of high-quality EOS points are available to make the required interpolation and differentiation of  $E$  and  $P$  with respect to temperature satisfactorily accurate.

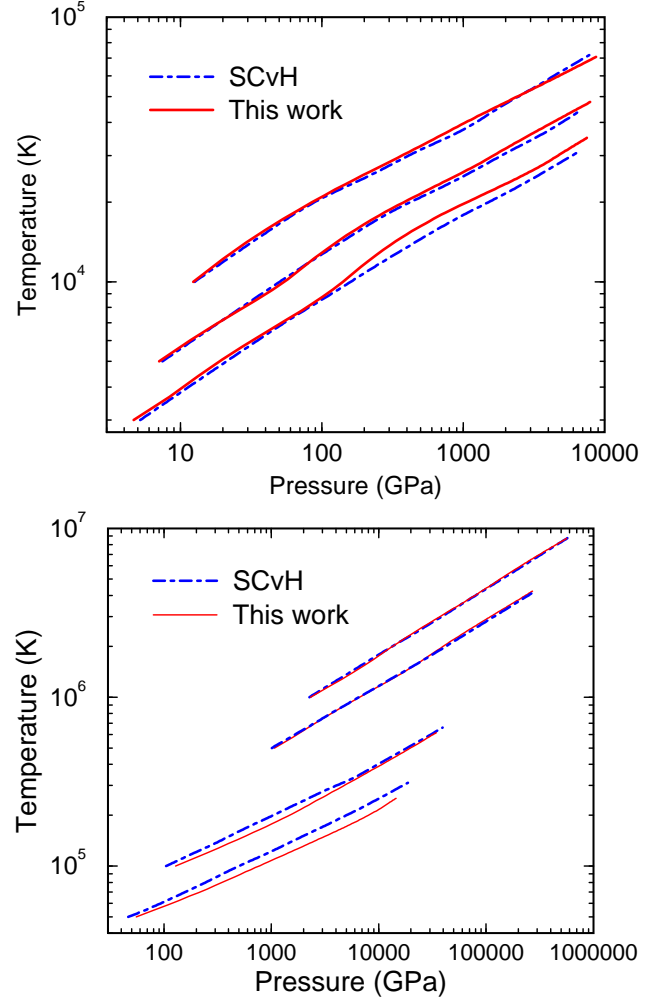


FIG. 12: Comparison in temperature-pressure space of the adiabats shown in Fig. 11.

One drawback of formula (5) is that it is not necessarily thermodynamically consistent if pressures and internal energies are interpolated separately. This is the primary reason why we developed the following method to fit the free energy instead. Pressure and internal energy are related to the free energy,  $F(V, T)$ , by

$$P = - \left. \frac{\partial F}{\partial V} \right|_T \quad \text{and} \quad E = F - T \left. \frac{\partial F}{\partial T} \right|_V. \quad (6)$$

Different EOS fits for fluids have been proposed in the literature<sup>36,43</sup>. Thermodynamic consistency was not a priority in each case. Both papers relied on specific functional forms that were carefully adjusted to the material under consideration. Although such a fit of specific form could probably have also been constructed for the presented helium EOS data, we wanted to have an approach that is not just applicable to one material. Therefore, we decided to represent the free energy as a bi-cubic spline function with temperature and density as parameters. This spline function can accurately represent our helium

EOS data and can easily be adapted to fit other materials. Cubic splines are twice continuously differentiable, which means the derived pressures and energies are once continuously differentiable with respect to  $V$  and  $T$ . This is sufficient for this study. If additional thermodynamic functions that require higher order derivatives of the free energy, such as sound speeds, need to be fit also then higher order splines can accommodate that.

We start the free energy interpolation by constructing as series of one-dimensional splines functions  $F_n(T)$  for different densities. The choice of knots  $T_i$  is arbitrary. Their location should be correlated with the complexity of the EOS as well as the distribution of EOS data points. In our helium example, we used a logarithmic grid in temperature with about half as many knots as data points. The set of free energy values on the knots,  $F(T_i)$ , represent the majority of the set of fit parameters. In addition, one may also include the first derivatives of the splines  $\frac{\partial F_n}{\partial T}|_V$  at the lowest and highest temperature, which represent the entropy. Alternatively, one could derive those derivatives by other means and then keep them fixed during the fitting procedure.

To compute the free energy at a specific density,  $n^*$ , and temperature,  $T^*$ , we first evaluate all splines  $F_n(T^*)$  and then construct a secondary spline at constant temperature as function of density,  $F_{T^*}(n)$ . Its first derivative is related to the pressure. Again, the derivative at the interval boundaries can either be fixed or adjusted during the fitting procedure. We adjust them by introducing an additional spline  $\frac{\partial F}{\partial n}|_T(T)$  at the lowest and highest densities, which then get adjusted in the fitting procedure.

We begin the fitting procedure with an initial guess for the free energy function derived from Eq. (5). Then we employ conjugate gradient methods<sup>44</sup> to optimize the whole set of fitting parameters. Minimizing the sum of the squared relative deviations in pressure and internal energy has been found to work best. (Just for the derivation of the relative deviation in energy, the zero of energy has been shifted to value of the isolated helium atom.)

All fits tend to introduce wiggles if too many free parameters are included. We control wiggles by adjusting the number of knots in density and temperature but we also introduced penalty in the form,

$$\xi = \int d\rho \left( \frac{\partial^3 F}{\partial n^3} \right)^2, \quad (7)$$

to favor fits with smaller  $|\partial^2 P / \partial n^2|$ . Finally we changed the density argument in the spline interpolation from  $F_T(\rho)$  to  $F_T(\log(\rho))$ . This improves the fit in the high temperature limit where the free energy is dominated by the ideal gas term that has logarithmic dependence on density.

The presented free energy fit is thermodynamically consistent by construction. It allowed us to accurately represent the entire data set of  $P$  and  $E$  values. Without additional information, the free energy can be determined up to a term  $T\Delta S$ , which is sufficient to compute adiabats. To determine the absolute value of the entropy, one

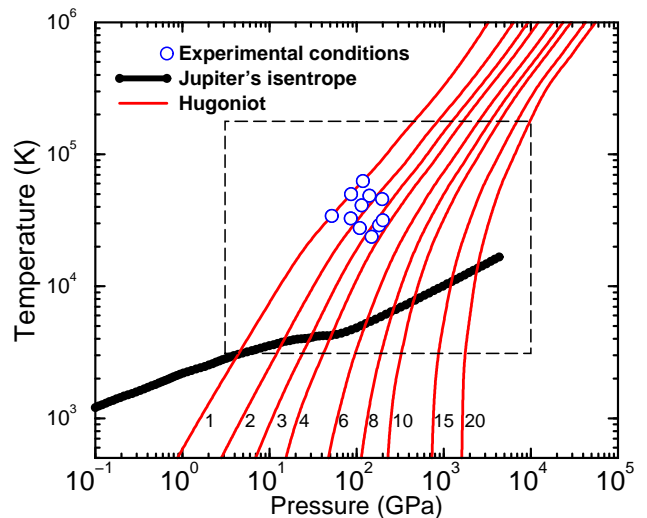


FIG. 13: Comparison of Jupiter's isentrope with helium shock Hugoniot curves for different precompression ratios. The labels specify the precompression ratio relative to the density at ambient pressures ( $\rho_0 = 0.1235 \text{ g cm}^{-3}$ , Ref.<sup>16</sup>). The symbols approximately represent recent experiments<sup>18</sup>. The inside of the dashed box indicates conditions, for which the SCvH EOS<sup>41</sup> was interpolated and is not thermodynamically consistent.

needs an anchor point, for which the entropy was derived by different means.

Figure 11 compares different adiabats derived from our first-principles EOS with predictions from the SCvH EOS model. Beginning from a joint starting point of  $r_s = 2.4$  and a selection of seven different temperatures of 3000, 5000, 10 000, 50 000, 100 000, 500 000, and  $10^6$  K, we constructed the adiabats for both models for the density interval under consideration. The upper panel of Fig. 11 demonstrates good agreement between both methods a low densities up to about  $1 \text{ g cm}^{-3}$ . For higher densities, one finds deviations of up to 20% in the predicted temperatures on the adiabat. A higher temperature, the agreement get substantially better, which is illustrated in the lower panel of Fig. 11. The observed deviations are similar to pressure differences shown in Fig. 6.

For applications in the field of planetary science, we also show the adiabats in  $(T, P)$  space in Fig. 12. The deviations are comparable in magnitude but appear smaller on a logarithmic scale.

## VI. SHOCK WAVE EXPERIMENTS

Dynamic shock compression experiments are the preferred laboratory experiments to probe the properties materials at high pressure and temperature. Using bigger and more powerful lasers, great progress has been made in reaching higher and higher pressures. Under shock compression, the initial state of material characterized by internal energy, pressure, and volume ( $E_0, P_0, V_0$ )

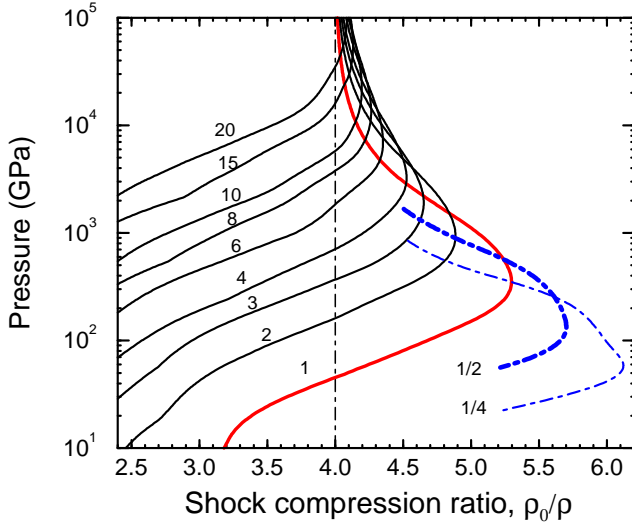


FIG. 14: Hugoniot curves for different precompression ratios from Fig. 13 plotted as function of shock compression.

changes to the final state described by  $(E, P, V)$ . The conservation of mass, momentum, and energy yields the Hugoniot condition<sup>45</sup>,

$$H = (E - E_0) + \frac{1}{2}(P + P_0)(V - V_0) = 0. \quad (8)$$

Different shock velocities lead to a collection of final states that are described by a Hugoniot curve. Using Eq. 8, this curve can easily be calculated for a given EOS where one most often may assume  $P_0 \ll P$ .  $V_0 = 32.4 \text{ cm}^3/\text{mol}$  ( $\rho_0 = 0.1235 \text{ g cm}^{-3}$ ) is taken from experiment<sup>16</sup>. For  $E_0$ , one takes the energy of an isolated helium atom, which must be calculated consistently with the final internal energy,  $E$ . An initial static precompression that changes  $V_0$  will also affect  $E_0$  and  $P_0$  but the corrections are negligible as long as the amount of initial compression work is small compared to the energy that is deposited dynamically. Assuming  $dE_0 = dP_0 = 0$ , the total differential of  $H$  reads,

$$dH = dE + \frac{P}{2}dV - \frac{P}{2}dV_0 + \frac{1}{2}(V - V_0)dP \quad (9)$$

The point of maximum compression,  $\eta_{\max} = V_0/V$ , along the Hugoniot curve can be derived by setting,  $dH = dV = dV_0 = 0$ . The resulting condition can be expressed in terms of the Grüneisen parameter,  $\gamma \equiv V \frac{\partial P}{\partial E} \Big|_V = 2/(\eta_{\max} - 1)$ .

Now we will determine how the maximum compression ratio,  $\eta_{\max}$ , changes if the sample is precompressed statically. Keeping the final shock pressure constant, the compression ratio changes as function of the initial sample volume,  $V_0$ ,

$$\frac{\partial \eta}{\partial V_0} \Big|_P = \frac{1}{V} - \frac{V_0}{V^2} \frac{\partial V}{\partial V_0} \Big|_P. \quad (10)$$

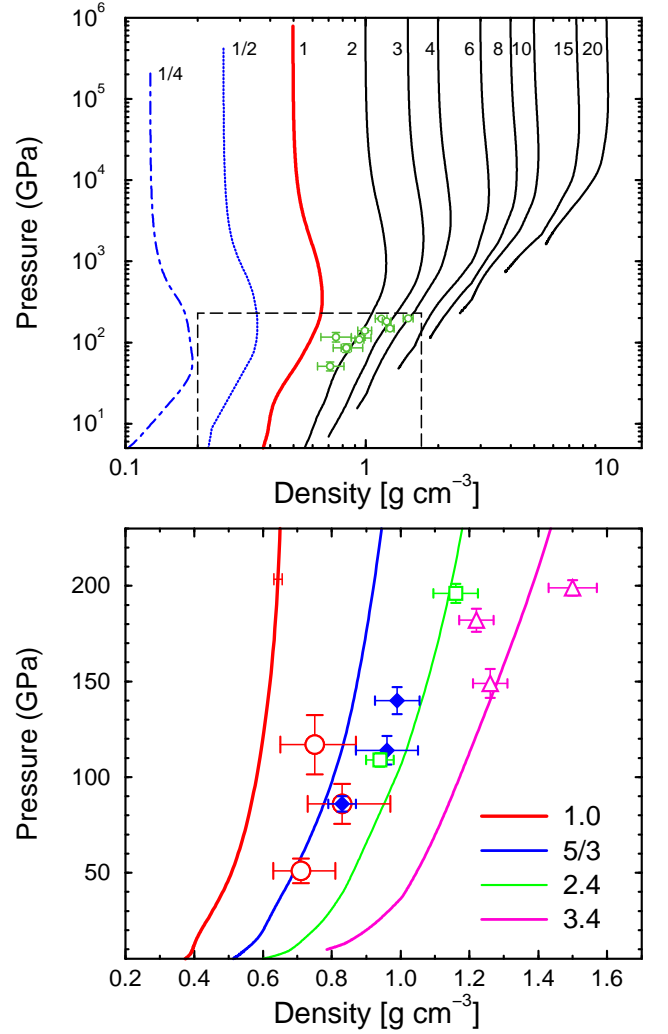


FIG. 15: Pressure-density plot of shock Hugoniot curves for different precompression ratios. The upper panel shows the shock Hugoniot curves from Fig. 14, recent experimental results (symbols), and the range of the lower plot. Below we plot the Hugoniot curves for precompression ratios (see labels) that approximately match the experimental conditions (symbols, see Ref.<sup>18</sup>). The error bar on the upper left solid line represents the uncertainty in the calculations.

Setting  $dH = dP = 0$  in Eq. 9, one finds,

$$\frac{\partial V_0}{\partial V} \Big|_P = \frac{2}{P} \frac{\partial E}{\partial V} \Big|_P + 1 \equiv \frac{2}{\delta} + 1. \quad (11)$$

Inserting this result into Eq. 10 yields,

$$V \frac{\partial \eta_{\max}}{\partial V_0} \Big|_P = \frac{2(\gamma - \delta)}{\gamma(2 + \delta)}. \quad (12)$$

Since the parameters  $\gamma$  and  $\delta$  are both positive, the relation,  $\frac{\partial \eta_{\max}}{\partial V_0} \Big|_P > 0$ , is equivalent to the relation,  $\delta < \gamma$ , which is again equivalent to,

$$1 < \frac{\rho}{P} \frac{\partial P}{\partial \rho} \Big|_E. \quad (13)$$

If this condition is fulfilled for a particular EOS then the maximum shock compression ratio will decrease if the sample is precompressed statically, which reduces  $V_0$ . We have computed the isoenergetic compressibility for our first-principles EOSs for helium and hydrogen and verified that this condition is satisfied for both materials (Fig. 14). It is also fulfilled for an ideal plasma model because the maximum compression ratio is determined by the balance of excitations of internal degrees of freedom and interaction effects<sup>17</sup>. Although all interactions are neglected, an ideal model correctly represents the fact the excited states are suppressed at high density because of the reduced entropy. The diminished importance of excitations reduces the maximum compression ratio to values closer to 4, which is the expected result for non-interacting systems without internal degrees of freedom.

Recent laser shock wave experiments<sup>18</sup> reached pressures of 2 megabars in fluid helium for the first time. The sample was precompressed statically in a modified diamond anvil cell before the shock was launched. The static precompression is an important development that enables one to reach higher densities and still allows one to directly determine the EOS. Reaching higher densities is important for planetary interiors because shock Hugoniot curves rise faster than adiabats in a  $P$ - $T$  diagram shown in Fig. 13. As a result, a large part of Jupiter's adiabat remains inaccessible unless one increases the starting density by precompression. The precompression and relation of planetary interiors was studied theoretically in Ref.<sup>46</sup>. It was demonstrated that precompression of up to 60 GPa would be needed to characterize 50% of Jupiter's envelope. The challenge is here to reach high enough densities because a single shock wave compresses the material only 5.25-fold or less (Fig. 14).

The measurements of J. Eggert *et al.*<sup>18</sup> confirmed two of our theoretical predictions<sup>17</sup>. They showed that helium has a shock compression ratio substantially larger than 4 due to the electronic excitations and that the compression ratio would decrease with increasing precompression (Fig. 14). However, the measurements appeared to be in better agreement with the SCvH EOS model than PIMC simulations<sup>18</sup>. The SCvH model predicts a maximum compression ratio of 6.5 to occur around 300 GPa. A different chemical model based on an expansion of the activity<sup>47</sup> predicts maximum compression ratios between 5.6 and 6.2 to occur at about 100 GPa.

Figure 15 shows a detailed comparison between experiments and our first-principles simulations. The shock measurements without precompression indeed show a

higher compression than predicted from first principles. The deviations are outside the experimental error bars. However, this discrepancy goes away with increasing precompression. The shocks with 3.4-fold precompression are in good agreement with first-principles predictions. We have no explanation for this trend at present.

The reason why the SCvH EOS yields larger compression ratios can be understood by looking at the pressure that this model predicts. Using our first-principles EOS, we derived the shock temperatures that correspond to the reported  $P$ - $\rho$  measurements. In the resulting temperature range of 24 000 – 63 000 K, the SCvH EOS significantly underestimates the pressure (see Fig. 6), which leads to higher predicted compressions (Eq. 8). Furthermore, all measurements fall in the region where the SCvH model relied on interpolation (Fig. 13) and is not expected to be as reliable.

## VII. CONCLUSIONS

This paper combined path integral Monte Carlo and density functional molecular dynamics simulation to derive one coherent equation of state for fluid helium at high pressure and temperature. Helium is a comparatively simple material since it does not form chemical bonds nor has core electrons, but our approach of combining two simulation techniques can be generalized to study more complex materials at extreme conditions. Certainly the presented approach to fit the free energy and to derive adiabats works for any set of EOS data points derived from first-principles simulations.

For the future, one might consider replacing DFT-MD with coupled ion-electron Monte Carlo<sup>48</sup>. However this is strictly a groundstate method and one would still need to find a way to include electronic excitations.

## Acknowledgments

This material is based upon work supported by NASA under the grant NNG05GH29G and by the NSF under the grant 0507321. We thank D. Saumon for providing us with his He EOS table<sup>41</sup>, and acknowledge receiving the preliminary manuscript<sup>21</sup> from L. Stixrude and R. Jeanloz. We thank the authors of ref.<sup>18</sup> for sending us a table with their experimental results.

<sup>1</sup> D.J. Stevenson and E.E. Salpeter. *Astrophys. J. Suppl. Ser.*, 35:221, 1977.

<sup>2</sup> D.J. Stevenson and E.E. Salpeter. *Astrophys. J. Suppl.*, 35:239, 1977.

<sup>3</sup> H.-K. Mao et al. *Phys. Rev. Lett.*, 60:2649, 1988.

<sup>4</sup> P. Loubeyre, R. LeToullec, J. P. Pinceaux, H. K. Mao,

J. Hu, and R. J. Hemley. *Phys. Rev. Lett.*, 71:2272, 1993.

<sup>5</sup> D. A. Young, A. K. McMahan, and M. Ross. *Phys. Rev. B*, 24:5119, 1981.

<sup>6</sup> P. M. Kowalski, S. Mazevet, D. Saumon, and M. Challacombe. *Phys. Rev. B*, 76:075112, 2007.

<sup>7</sup> L. B. Da Silva *et al.* *Phys. Rev. Lett.*, 78:483, 1997.

- <sup>8</sup> G. W. Collins *et al.* *Science*, 281:1178, 1998.
- <sup>9</sup> M. D. Knudson *et al.* *Phys. Rev. Lett.*, 87:225501, 2001.
- <sup>10</sup> M. D. Knudson, D. L. Hanson, J. E. Bailey, C. A. Hall, and J. R. Asay. *Phys. Rev. Lett.*, 90:035505, 2003.
- <sup>11</sup> S.I. Belov *et al.* *JETP Lett.*, 76:443, 2002.
- <sup>12</sup> G. V. Boriskov *et al.* *Phys. Rev. B*, 71:092104, 2005.
- <sup>13</sup> T. J. Lenosky, J. D. Kress, and L. A. Collins. *Phys. Rev. B*, 56:5164, 1997.
- <sup>14</sup> B. Militzer and D. M. Ceperley. *Phys. Rev. Lett.*, 85:1890, 2000.
- <sup>15</sup> S. A. Bonev, B. Militzer, and G. Galli. *Phys. Rev. B*, 69:014101, 2004.
- <sup>16</sup> W. J. Nellis *et al.* *Phys. Rev. Lett.*, 53:1248, 1984.
- <sup>17</sup> B. Militzer. *Phys. Rev. Lett.*, 97:175501, 2006.
- <sup>18</sup> J. Eggert *et al.* *Phys. Rev. Lett.*, 100:124503, 2008.
- <sup>19</sup> A. Kietzmann, B. Holst, R. Redmer, M. P. Desjarlais, and T. R. Mattsson. *Phys. Rev. Lett.*, 98:190602, 2007.
- <sup>20</sup> V. Ya. Ternovoi *et al.* *AIP Conf. Proc.*, 620:107, 2002.
- <sup>21</sup> L. Stixrude and R. Jeanloz. Fluid helium at conditions of giant planet interiors. Submitted to *Proc. Nat. Ac. Sci.* (2008).
- <sup>22</sup> D. M. Ceperley. *Rev. Mod. Phys.*, 67:279, 1995.
- <sup>23</sup> E. L. Pollock. *Comp. Phys. Comm.*, 52 :49, 1988.
- <sup>24</sup> V. Natoli and D. M. Ceperley. *J. Comp. Phys.*, 117:171–178, 1995.
- <sup>25</sup> B. Militzer and R. L. Graham. *Journal of Physics and Chemistry of Solids*, 67:2143, 2006.
- <sup>26</sup> D. M. Ceperley. *J. Stat. Phys.*, 63:1237, 1991.
- <sup>27</sup> D. M. Ceperley. Editrice Compositori, Bologna, Italy, 1996.
- <sup>28</sup> B. Militzer and E. L. Pollock. *Phys. Rev. E*, 61:3470, 2000.
- <sup>29</sup> CPMD, Copyright IBM Corp 1990-2006, MPI für Festkörperforschung Stuttgart 1997-2001.
- <sup>30</sup> N. Troullier and J. L. Martins. *Phys. Rev. B*, 43:1993, 1991.
- <sup>31</sup> G. Kresse and J. Hafner, *Phys. Rev. B* 47, 558 (1993); G. Kresse and J. Hafner, *Phys. Rev. B* 49, 14251 (1994); G. Kresse and J. Furthmüller, *Comput. Mat. Sci.* 6, 15 (1996); G. Kresse and J. Furthmüller, *Phys. Rev. B* 54, 11169 (1996).
- <sup>32</sup> P. E. Blöchl. *Phys. Rev. B*, 50:17953, 1994.
- <sup>33</sup> J. P. Perdew, K. Burke, and M. Ernzerhof. *Phys. Rev. Lett.*, 77:3865, 1996.
- <sup>34</sup> R.A. Aziz, A.R. Janzen, and M. R. Moldover. *Phys. Rev. Lett.*, 74:1586, 1995.
- <sup>35</sup> B. Militzer and E. L. Pollock. *Phys. Rev. B*, 71:134303, 2005.
- <sup>36</sup> G. S. Stringfellow, H. E. DeWitt, and W. L. Slattery. *Phys. Rev. A*, 41:1105, 1990.
- <sup>37</sup> B. Militzer and D. M. Ceperley. *Phys. Rev. E*, 63:066404, 2001.
- <sup>38</sup> O. H. Nielsen and R. M. Martin. *Phys. Rev. B*, 32:3780, 1985.
- <sup>39</sup> P. Debye and E. Hückel. *Phys. Z.*, 24:185, 1923.
- <sup>40</sup> C. Winisdoerffer and G. Chabrier. *Phys. Rev. E*, 71:026402, 2005.
- <sup>41</sup> D. Saumon, G. Chabrier, and H. M. Van Horn. *Astrophys. J. Suppl.*, 99:713, 1995.
- <sup>42</sup> D. Saumon and G. Chabrier. *Phys. Rev. A*, 46:2084, 1992.
- <sup>43</sup> T. J. Lenosky, S. R. Bickham, J. D. Kress, and L. A. Collins. *Phys. Rev. B*, 61:1, 2000.
- <sup>44</sup> W. H. Press, S. A. Teukolsky, W. T. Vetterling, and B. P. Flannery. *Numerical Recipes in C++*. Cambridge University Press, Cambridge, UK, 2001.
- <sup>45</sup> Y. B. Zeldovich and Y. P. Raizer. Academic Press, New York, 1966.
- <sup>46</sup> B. Militzer and W. B. Hubbard. *AIP Conf. Proc.*, 955:1395, 2007.
- <sup>47</sup> M. Ross, F. Rogers, N. Winter, and G. Collins. *Phys. Rev. B*, 76:020502(R), 2007.
- <sup>48</sup> K. T. Delaney, C. Pierleoni, and D. M. Ceperley. *Phys. Rev. Lett.*, 97:235702, 2006.

## APPENDIX A: FREE ENERGY SPLINE INTERPOLATION

We constructed the following 2D spline interpolation of the free energy in order to reproduce the internal energy and pressures from Tab. I. We use atomic units of Hartrees and Bohr radii. For each density of  $r_s = \{2.4, 2.0, 1.6, 1.2, 0.8\}$ , we construct a cubic spline  $F_n(T)$ . Table VI lists 16 knot points  $(T_i, F(T_i))$  for each density. In addition, the first derivative  $\frac{\partial F}{\partial T}$  are specified at the lowest and highest temperatures. This is sufficient to construct a cubic spline function  $F(T)$ <sup>44</sup>.

In a similar fashion, we derive a spline function that contains that free energy derivative with respect to density,  $\frac{\partial F}{\partial n}(T)$ , at the lowest and highest densities,  $r_s = 2.4$  and 0.8 respectively.  $n$  is the density of the electrons,  $n = N_e/V$ . Those knot points as well as the  $T$  derivatives are included in Tab. VI also.

In order to obtain the free energy for a particular density and temperature,  $(n^*, T^*)$ , we proceed as follows. First we evaluate the spline functions  $F(T^*)$  and  $\frac{\partial F}{\partial n}(T^*)$  at temperature  $T^*$ . Using these five knots points and density derivatives, we construct a spline function,  $F(\log(n))$ . We use  $\log(n)$  as argument because it better represents the high-temperature limit of weak interactions. Note that the constructed splines for the density derivative contain  $\frac{\partial F}{\partial n}$  and not  $\frac{\partial F}{\partial \log(n)}$ . Then  $F(\log(n))$  is evaluated at the density of interest,  $n^*$ . Finally we add the term,  $-T\Delta S = -13.7902836 \text{ Ha} \cdot T$ , which brings the entropy in agreement with our Debye-Hückel reference point at high temperature for  $r_s=1.86$ . This procedure yields the free energy  $F(n^*, T^*)$  in Hartrees per electron. Other thermodynamic variables including pressure, internal energy, entropy, and Gibbs free energy can be obtained by differentiation.

TABLE VI: Knot points for free energy spline interpolation

$T(\text{a.u.})$	$f(r_s = 2.4, T)$	$f(r_s = 2.0, T)$	$f(r_s = 1.6, T)$	$f(r_s = 1.2, T)$	$f(r_s = 0.8, T)$
0.001583407607	-1.433567121	-1.431135811	-1.422237604	-1.377317056	-1.089747214
0.004369348882	-1.406243368	-1.402248169	-1.390358674	-1.34121764	-1.049220122
0.01205704051	-1.338444742	-1.330719999	-1.313137294	-1.255091313	-0.9491949603
0.03327091284	-1.169814789	-1.154154406	-1.125146478	-1.047701304	-0.7135001905
0.09180973061	-0.7578793569	-0.7214892496	-0.6653645937	-0.5501514183	-0.1583196636
0.2533452171	0.1213432393	0.2279596473	0.3697481593	0.5961317377	1.145222958
0.6990958211	1.448161918	1.849742465	2.331720062	2.967152398	4.011622282
1.929126481	1.650153009	3.082886945	4.795803813	6.956651264	9.947352284
5.323346054	-6.480107758	-2.223161966	2.964697691	9.579180258	18.74636894
14.6895569	-50.37972679	-38.41515844	-23.79211621	-4.992619324	21.39894481
40.53523473	-231.4313924	-198.2806566	-157.6765535	-105.3657984	-31.61456362
111.8553314	-893.7314032	-802.1449141	-689.7861073	-544.9061891	-340.7935545
308.660237	-3172.519712	-2918.919455	-2608.696846	-2207.77895	-1644.63782
851.7353686	-10693.37579	-9996.590015	-9137.681211	-8032.176108	-6477.239292
2350.329104	-34893.6373	-32971.41578	-30600.55572	-27552.36594	-23259.81241
6485.637557	-111050.5942	-105746.9466	-99203.62441	-90788.1102	-78945.99564
$f'(r_s, T_1)$	10.43646526	10.93007841	12.42958105	14.04097874	13.75171132
$f'(r_s, T_N)$	-19.3620206	-18.54727965	-17.53417624	-16.23883073	-14.41224513

$T(\text{a.u.})$	$\frac{\partial f}{\partial n}(r_s = 2.4, T)$	$\frac{\partial f}{\partial n}(r_s = 0.8, T)$
0.001583407607	0.1605721538	0.9460950728
0.004369348882	0.2923651353	0.9625433841
0.01205704051	0.6458549976	0.9782855175
0.03327091284	1.463747273	1.029890765
0.09180973061	3.574255133	1.142591093
0.2533452171	10.98479122	1.409424435
0.6990958211	43.27443042	2.089943658
1.929126481	153.211445	5.309130852
5.323346054	450.4159975	15.9843674
14.6895569	1263.720981	46.33079487
40.53523473	3502.359609	129.8984992
111.8553314	9679.619949	359.8256334
308.660237	26719.83852	992.5003633
851.7353686	73736.1465	2741.461026
2350.329104	203474.5198	7568.332998
6485.637557	561480.8894	20879.15481
$f'(r_s, T_1)$	47.35562925	6.453623893
$f'(r_s, T_N)$	86.57538487	3.218499127

TABLE VII: Reduced coordinates of the DFT-MD configuration with 57 atoms that was used to report the  $r_s = 1.86$  results for the instantaneous pressure in Fig. 4. The cell size is  $L = 14.5382$  a.u.

$x/L$	$y/L$	$z/L$	$x/L$	$y/L$	$z/L$
0.749029	0.334272	0.723992,	0.359050	0.631169	0.090795
0.636183	0.917961	0.531890,	0.500277	0.715818	0.420142
0.509121	0.642554	0.328933,	0.192192	0.222632	0.042651
0.273631	0.845722	0.363632,	0.070837	0.830223	0.693497
0.053785	0.837401	0.054990,	0.138489	0.091713	0.097622
0.250609	0.517490	0.740851,	0.953625	0.430789	0.067921
0.107008	0.407958	0.463387,	0.023708	0.960709	0.487179
0.988548	0.830572	0.241931,	0.811738	0.062550	0.902069
0.244399	0.482412	0.399190,	0.693258	0.647174	0.360832
0.924284	0.678572	0.470508,	0.181701	0.886709	0.333868
0.780287	0.033015	0.620919,	0.859185	0.932541	0.252564
0.774645	0.083064	0.349744,	0.903457	0.888628	0.124621
0.293881	0.081041	0.053630,	0.220134	0.760599	0.688370
0.493690	0.930407	0.343378,	0.585411	0.439278	0.167284
0.648043	0.965342	0.702852,	0.219455	0.957094	0.895428
0.504966	0.639074	0.084498,	0.906610	0.508304	0.938057
0.716468	0.854022	0.986517,	0.385839	0.307391	0.681601
0.099368	0.291429	0.740170,	0.475139	0.160612	0.598743
0.252564	0.696499	0.576596,	0.788211	0.564812	0.486616
0.613177	0.259980	0.238984,	0.296858	0.344416	0.229757
0.526564	0.816547	0.598836,	0.429733	0.712523	0.742929
0.507514	0.904602	0.268688,	0.685066	0.562001	0.926251
0.614731	0.263859	0.402947,	0.432246	0.210193	0.939664
0.115992	0.498747	0.676389,	0.424152	0.141821	0.676522
0.778767	0.981750	0.935757,	0.208696	0.768371	0.292528
0.334815	0.183086	0.275601,	0.487257	0.590889	0.227333
0.975542	0.456665	0.257836,	0.577884	0.835181	0.876629
0.737370	0.699890	0.544111,	0.177496	0.781162	0.853225
0.558513	0.066648	0.194491			